

# Aspect Ratio-Dependent Dynamics of Piezoelectric Transducers in Wireless Acoustic Power Transfer

Ahmed Allam<sup>®</sup>, Karim G. Sabra, and Alper Erturk<sup>®</sup>

Abstract—Acoustic power transfer (APT) for wireless electronic components has received growing attention as a viable approach to deliver power to remotely located small electronic devices. The design of an efficient APT system requires accurate models to describe its individual components as well as the interaction between them. Most of the analytical models available to represent the bulk piezoelectric transducers used in APT are limited to either thin rod or thin plate transducers. However, transducers with moderate aspect ratios are often used, especially at the receiver end. In this work, in addition to reviewing standard theories, models based on the Rayleigh and Bishop rod theories are developed to analyze transducers [transmitter (TX) or receiver (RX)] with various aspect ratios. Results from these models are compared with experimental data and finite-element analysis to determine the range of aspect ratios in which they are valid. In addition, fluid loading effects on the predictions of all models are investigated, and the generated pressure fields by the transducers with different aspect ratios are compared. The resulting models are used to analyze the effect of aspect ratio on the performance of the transducer when operated as a TX or an RX in an APT setting.

Index Terms—Acoustics, piezoelectric, transducers, wireless power transfer.

### I. INTRODUCTION

IRELESS electronic devices in the form of embedded sensing, communication, and actuation modules are used in a wide range of engineering applications. These devices usually require minimal power to operate, but they are often placed in remote, hazardous, or inaccessible locations. Their presence in such locations prevents powering via wires and require other practical means for power delivery. When sufficient usable energy is present in the ambient environment, it could be collected and converted to electrical energy using energy-harvesting devices [1]–[6]. However, if the ambient energy is limited, external energy can be supplied to these electronic devices using a wireless power transfer system. Such a system consists of a transmitter (TX) connected to

Manuscript received September 28, 2019; accepted December 23, 2019. Date of publication December 27, 2019; date of current version April 24, 2020. This work was supported by the National Science Foundation CMMI grant 1727951. (Corresponding author: Ahmed Allam.)

The authors are with the G. W. Woodruff School of Mechanical Engineering, Georgia Institute of Technology, Atlanta, GA 30332 USA (e-mail: a.allam@gatech.edu).

Digital Object Identifier 10.1109/TUFFC.2019.2962711

an electric power source/circuit and a receiver (RX) that is integrated into the electronic device to be powered. TX converts the source electric power into another form of power (e.g., electromagnetic or acoustic), which can travel through the medium. RX then captures this power and converts it back to usable electric power usually through a signal conditioning circuit. The nature of the medium through which power is transferred, the electric load characteristics, and the separating distance between TX and RX are among the main factors to be considered when selecting how the power will be transmitted and, hence, the type of the transducers used as TX and RX. When the separating distance is small and the medium is air, electromagnetic transduction in the form of magnetic coupling is a popular approach to transfer energy between TX and RX [7]–[9]; however, the energy transfer efficiency of magnetically coupled transducers is reduced drastically with increased separation distance compared with TX and RX dimensions [10]. Moreover, certain applications impose limitations on the maximum amplitude of the electromagnetic waves used for power transfer that then limits the use of this transduction mechanism [11]. On the other hand, acoustic power transfer (APT) has found applications in powering biomedical implants [12], transmitting energy through metallic walls [13]-[15], and powering wireless sensors along industrial pipelines [16], [17] among others.

In a typical APT system (see Fig. 1), piezoelectric transducers are the most popular choice to convert electric power into acoustic waves and then back to electric power at the receiving end. The height (or thickness) of the transducer (h) dominantly controls its operating frequency range at which maximum acoustic-to-electric power conversion (or vice versa) takes place. A low resonance frequency is preferred for reduced attenuation of propagating wave energy, but this requires a thicker transducer. Piezoelectric transducers operating around 1 MHz are usually a few millimeters thick, while those operating around 100 kHz could be as thick as a few centimeters for efficient operation. Transducers that generate a focused ultrasonic beam in an open medium generally need to have a large radius (a) relative to their thickness making platelike transducers a popular choice for ultrasonic TX design. The relationship between the transducer thickness, radius, operating frequency, and directionality requires a careful investigation of the effect of transducer's aspect ratio on its

0885-3010 © 2019 IEEE. Personal use is permitted, but republication/redistribution requires IEEE permission. See http://www.ieee.org/publications standards/publications/rights/index.html for more information.

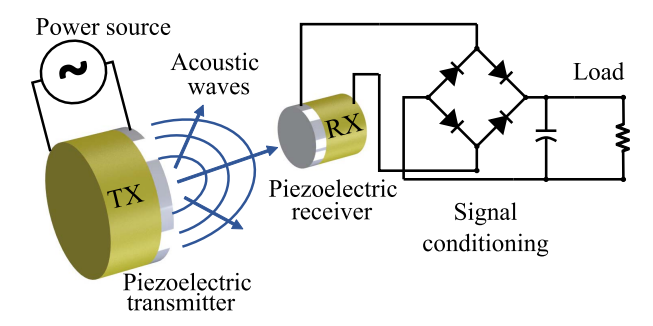


Fig. 1. Schematic of a typical wireless APT system.

performance, as well as its ability to function as a TX or an RX in wireless power transfer.

Several analytical techniques exist in the literature to model piezoelectric transducers. Perhaps the most common of them are Krimholtz, Leedom, and Matthae (KLM) and Mason [18] type of equivalent circuit models. These equivalent circuit models are convenient and easily simulated using available circuit analysis tools [19]; however, their accuracy and applicability depend on the dimensions of the transducer, specifically its aspect ratio ( $\beta = h/a$ ), unless the model parameters are identified from experiments. When derived from first principles (rather than being identified from experiments), KLM and Mason models are best suited for extreme aspect ratios: the thickness expander plate (thin infinite plate assumption) that can be only used for very small  $\beta$  or the length expander bar that can be only used for very large  $\beta$ . These assumptions are difficult to satisfy when there are size limitations on the dimensions of the receiver, as for many of the suggested APT systems, size, and frequency constraints lead to transducers with moderate aspect ratios [20]-[23]. Analytical models based on the continuum dynamics of the transducers have also been investigated [24]–[27]. While these models offer insights into the factors affecting the power conversion capabilities of the transducers, their applicability is limited to transducers with extreme aspect ratios. To overcome these limitations experimentally, the parameters of both the equivalent circuit and analytical models are usually fit to the response of the actual transducers when they cannot be accurately modeled as a thin bar or a thin plate. This limits the usefulness of such models when the actual response of the transducer is critical to the performance of the APT system and prevents optimizing the system in the design phase.

Recently, we explored several continuum analytical models to approximate the response of a thickness-mode piezoelectric transducer, where each model is applicable within a specific range of aspect ratios [28]. The validity range of these models was investigated by comparing their numerical predictions to the values obtained using the finite-element method (FEM) simulations as well as experimental measurements of the impedance of thickness-mode PZT transducers. In this work, the introduced models are derived from basic principles, and the equations of the derived models are put in S-parameters (i.e., scattering parameters) matrix form, which can be easily imported to the abundantly available circuit simulators. This facilitates integrating their design with the other electrical

components involved in the APT system. The analytical and numerical methods are then used to analyze the effect of aspect ratio on the generated pressure field from the transducers when used as TX and the generated electrical power when used as RX.

In the following, dynamics of thickness-mode piezoelectric transducers are studied analytically, and transducer models based on the thin rod, Rayleigh (also known as Rayleigh-Love), Bishop (also known as Rayleigh-Bishop), and thin plate assumptions are derived using energy approaches in Section II. The impedance of each transducer is measured experimentally and compared with the analytical predictions and to numerical simulations in Section III. The effect of transducer's aspect ratio on its performance is analyzed when used as a transmitter in Section IV and as an RX in Section V. A summary of the findings of the work and concluding remarks are presented in Section VI.

# II. THICKNESS-MODE DYNAMICS OF A PIEZOELECTRIC TRANSDUCER WITH CIRCULAR CROSS SECTION

A continuum of piezoelectric material is governed by the piezoelectric constitutive equations that are given in their stress-charge form by

$$T = \mathbf{C}^E S - \mathbf{e}^T E \tag{1}$$

$$D = \mathbf{e}S + \epsilon^S E \tag{2}$$

where T and S are the mechanical stress and strain vectors, respectively, E and D are the electric field and electric displacement vectors, respectively,  $\mathbf{C}^E$  is the stiffness matrix at constant electric field,  $\boldsymbol{\epsilon}^s$  is the electric permittivity matrix at constant strain, and  $\mathbf{e}$  is the piezoelectric coupling matrix. Structural (mechanical) and dielectric losses are considered in the form of complex elastic and dielectric constants

$$\mathbf{C}^E = \mathbf{C}_{\text{undamped}}^E (1 - \gamma i), \quad \epsilon^S = \epsilon_{\text{undamped}}^S (1 - \delta i)$$

where  $\gamma$  and  $\delta$  are the structural and dielectric loss factors, respectively.

A cylindrical piezoelectric transducer with height h and radius a is considered [see Fig. 2(a)]. The transducer is poled in the longitudinal (z) direction, and thin metallic electrodes are deposited on its circular faces. The lateral components of the electric field and the electric displacement vanish; therefore, (1) and (2) can be simplified to

$$T_1 = C_{11}S_1 + C_{12}S_2 + C_{13}S_3 - e_{31}E_3 \tag{3}$$

$$T_2 = C_{12}S_1 + C_{22}S_2 + C_{13}S_3 - e_{31}E_3 \tag{4}$$

$$T_3 = C_{13}S_1 + C_{13}S_2 + C_{33}S_3 - e_{33}E_3 \tag{5}$$

$$T_4 = C_{44}S_4 \tag{6}$$

$$T_5 = C_{44}S_5 (7)$$

$$T_6 = \frac{C_{11} - C_{12}}{2} S_6 \tag{8}$$

$$D_3 = e_{31}S_1 + e_{31}S_2 + e_{33}S_3 + \epsilon_{33}E_3 \tag{9}$$

where the index 3 indicates the polarization direction, and (1,2) indicate the directions normal to the polarization vectors. Indices (4)–(6) follow the Voigt notation to represent shear

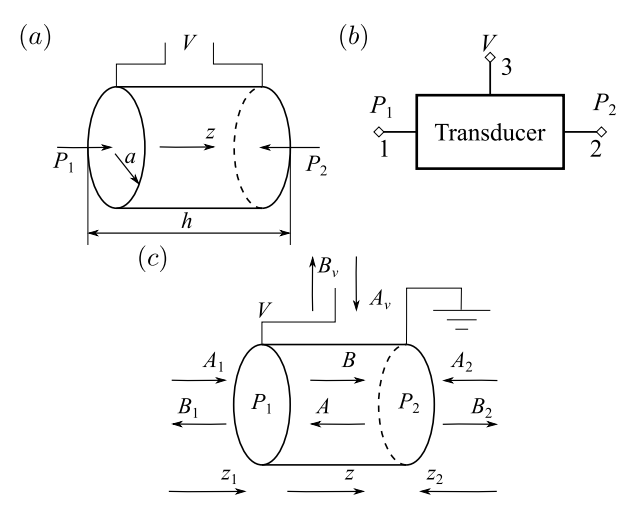


Fig. 2. (a) Schematic of a piezoelectric rod transducer. (b) Three-port element representation. (c) Incident and reflected voltage and pressure waves on the transducer.

stresses and strains. In the cylindrical coordinates  $(r, \theta, z)$ , the mechanical strain is related to the displacement field by [29]

$$S_{1} = \frac{du_{r}}{dr}, \quad S_{2} = \frac{1}{r} \left( \frac{du_{\theta}}{d\theta} + u_{r} \right), \quad S_{3} = \frac{du_{z}}{dz}$$

$$S_{4} = \frac{1}{r} \frac{du_{z}}{d\theta} + \frac{du_{\theta}}{dz}, \quad S_{5} = \frac{du_{r}}{dz} + \frac{du_{z}}{dr}$$

$$S_{6} = \frac{1}{r} \left( \frac{du_{r}}{d\theta} - u_{\theta} \right) + \frac{du_{\theta}}{dr}$$

$$(10)$$

where  $u_r$ ,  $u_\theta$ , and  $u_z$  are the displacements in the r-,  $\theta$ -, and z-directions, respectively. The modified Hamilton's principle for a piezoelectric volume is given by [30], [31]

$$\int_{t_1}^{t_2} \delta(\overline{T} - U + W_e + W_{nc}) dt = 0$$
 (11)

where  $\overline{T}$  is the total kinetic energy of the rod, U is the total potential (elastic) energy of the rod,  $W_e$  is the electric energy stored in the rod, and  $W_{nc}$  is the work due to the non-conservative forces acting on the rod including the external mechanical and electrical forces given by

$$\overline{T} = \frac{1}{2} \int_{\overline{V}} \rho \left( \dot{u}_r^2 + \dot{u}_\theta^2 + \dot{u}_z^2 \right) d\overline{V}$$
 (12)

$$U = \frac{1}{2} \int_{\overline{V}} \sum_{i=1}^{6} T_i s_i d\overline{V}$$
 (13)

$$W_e = \frac{1}{2} \int_{\overline{V}} E_3 D_3 d\overline{V} \tag{14}$$

$$W_{nc} = \int_{S} (\overline{t}_{r} u_{r} + \overline{t}_{\theta} u_{\theta} + \overline{t}_{z} u_{z} - \overline{q} \phi) dA$$
 (15)

where  $\rho$  is the mass density,  $\overline{V}$  is the volume, S is the external surface of the transducer,  $\overline{t}$  is the external traction acting on the surface of the transducer,  $\overline{q}$  is the external surface charge density, and  $\phi$  is the electric potential applied to the surface.

The response of the transducer cannot be estimated analytically unless certain assumptions are made regarding the displacement fields inside it. These assumptions can be made when the aspect ratio  $(\beta = (h/a))$  of the transducer is very

high (thin rod, Rayleigh, and Bishop theories) or very low (thickness vibration of an infinite plate).

#### A. Classical Thin Rod Model

For a symmetric thin rod, the lateral stresses and shear stresses are assumed to be very small, that is

$$T_1 = T_2 = T_4 = T_5 = T_6 = 0.$$
 (16)

The longitudinal displacement  $u_z$  is assumed to have the form

$$u_z = u(z, t) \tag{17}$$

and the electric potential  $\phi(z, t)$  is related to the electric field  $E_3$  by

$$E_3 = -\frac{\partial \phi}{\partial z}.\tag{18}$$

Substituting (16)–(18) into (3)–(9) and (10) yields

$$T_{3} = C_{33}u^{(1,0)}(z,t) + e_{33}\phi^{(1,0)}[z,t] - \frac{2C_{13}(C_{13}u^{(1,0)}(z,t) + e_{31}\phi^{(1,0)}(z,t))}{C_{11} + C_{12}}$$
(19)

$$D_{3} = e_{33}u^{(1,0)}(z,t) - \epsilon_{33}\phi^{(1,0)}(z,t) - \frac{2e_{31}(C_{13}u^{(1,0)}(z,t) + e_{31}\phi^{(1,0)}(z,t))}{C_{11} + C_{12}}$$
(20)

where the superscript (m, n) indicates the mth derivative with respect to z and the nth derivative with respect to t. Substituting (16)–(20) in (12)–(15) and neglecting the lateral inertia terms ( $\dot{u}_r = \dot{u}_\theta = 0$ ) yield the formula for the conserved energies inside the rod in terms of the longitudinal displacement u(z,t) and electric potential  $\phi(z,t)$ 

$$\overline{T} = \frac{1}{2} \int_{\overline{V}} \rho(u^{(0,1)}(z,t)^2) d\overline{V}$$

$$U = \frac{1}{2} \int_{\overline{V}} \left( \left( C_{33} - \frac{2C_{13}^2}{C_{11} + C_{12}} \right) u^{(1,0)}(z,t)^2 + \left( e_{33} - \frac{2C_{13}e_{31}}{C_{11} + C_{12}} \right) \phi^{(1,0)}(z,t) u^{(1,0)}(z,t) \right) d\overline{V}$$
(22)

(12) 
$$W_{e} = \frac{1}{2} \int_{\overline{V}} \left( \left( \epsilon_{33} + \frac{2e_{31}^{2}}{C_{11} + C_{12}} \right) \phi^{(1,0)}(z,t)^{2} - \left( e_{33} - \frac{2C_{13}e_{31}}{C_{11} + C_{12}} \right) u^{(1,0)}(z,t) \phi^{(1,0)}(z,t) \right) d\overline{V}.$$
(23)

For the rod shown in Fig. 2(a), the nonconservative work is given by

$$W_{nc} = P_1(t)u(0,t) + P_2(t)u(h,t) - Q(t)\phi(h,t)$$
 (24)

where Q(t) is the total electric charge flowing into or from the transducer's domain. Substituting (21)–(23) back into (11), taking the variation of the integral with respect to u(z,t) and  $\phi(z,t)$ , and performing integration by parts yields the electromechanical governing equations

$$\rho u^{(0,2)}(z,t) - \overline{C}u^{(2,0)}(z,t) + \overline{e}\phi^{(2,0)}(z,t) = 0$$
 (25)

$$\overline{e}u^{(2,0)}(z,t) - \overline{\epsilon}\phi^{(2,0)}(z,t) = 0 \quad (26)$$

and the boundary conditions

$$-A_p(\overline{C}u^{(1,0)}(z,t) + \overline{e}\phi^{(1,0)}(z,t)) + P_{1,2}(t) = 0|_{z=0,h}$$
 (27)

$$\delta u(z,t) = 0|_{z=0,h}$$
 (28)

$$A_p(\overline{e}u^{(1,0)}(z,t) - \overline{\epsilon}\phi^{(1,0)}(z,t)) - Q(t) = 0|_{z=0,h}$$
 (29)

$$\delta\phi(z,t) = 0|_{z=0,h} \quad (30)$$

where

$$\overline{C} = C_{33} - \frac{2C_{13}^2}{C_{11} + C_{12}}, \quad \overline{e} = e_{33} - \frac{2C_{13}e_{31}}{C_{11} + C_{12}}$$

$$\overline{\epsilon} = \epsilon_{33} + \frac{2e_{31}^2}{C_{11} + C_{12}}$$
(31)

and  $A_p$  is the cross-sectional area of the transducer. Equations (27) and (28) are the mechanical natural and essential boundary conditions, while (29) and (30) are the electrical natural and essential boundary conditions, respectively. The solution of (26) is obtained by integration

$$\phi(z,t) = \frac{\overline{e}}{\overline{\epsilon}}u(z,t) + c_1 z + c_2. \tag{32}$$

The value of  $c_1$  could be expressed by substituting (32) in the electrical natural boundary condition (29)

$$c_1 = \frac{Q(t)}{A_p \overline{\epsilon}}. (33)$$

The value of  $c_2$  is arbitrary since it represents the absolute electric potential. The potential difference between the electrodes is given by

$$V(t) = \phi(h, t) - \phi(0, t)$$

$$= \frac{h}{A_{P}\overline{\epsilon}}Q(t) + \frac{\overline{\epsilon}}{\epsilon}(u(h, t) - u(0, t)). \tag{34}$$

Substituting (26) in the first equation of motion [see (25)] yields the mechanical wave equation

$$\rho u^{(0,2)}(z,t) - \overline{C}^D u^{(2,0)}(z,t) = 0 \tag{35}$$

where  $\overline{C}^D = \overline{C} + (\overline{e}^2/\overline{\epsilon})$  is the reduced stiffness of the bar at constant charge (open-circuit conditions). Assuming harmonic plane-wave solution of the form

$$u(z,t) = A_u e^{i(\omega t - kz)} + B_u e^{i(\omega t + kz)}$$
(36)

where  $k=(\omega/c)$  is the wavenumber,  $\omega$  is the angular frequency of the wave,  $c=(\overline{C}^D/\rho)^{1/2}$  is the speed of sound in the transducer, and  $A_u$  and  $B_u$  are the complex amplitudes of the forward and backward traveling displacement waves. The value of  $A_u$  and  $B_u$  can be evaluated from the mechanical boundary conditions given by (27) or (28).

A more general approach, however, for the estimation of the response of the transducer is to consider it as a three-port element and focus on relating the inputs and outputs of these elements in a generic sense. In this approach, the interface matching conditions given by (27) and (28) and the electrical boundary conditions (34) can be used to express a scattering matrix that relates incident and reflected waves at each port (both electrical and mechanical waves). The transducer scattering matrix S is given by

$$\begin{bmatrix} B_1 \\ B_2 \\ B_\nu \end{bmatrix} = \mathbf{S} \begin{bmatrix} A_1 \\ A_2 \\ A_\nu \end{bmatrix} = \begin{bmatrix} S_{11} & S_{12} & S_{13} \\ S_{21} & S_{22} & S_{23} \\ S_{31} & S_{32} & S_{33} \end{bmatrix} \begin{bmatrix} A_1 \\ A_2 \\ A_\nu \end{bmatrix}$$
(37)

where  $A_1$ ,  $B_1$ ,  $A_2$ , and  $B_2$  are the incident and reflected pressure waves on faces 1 and 2, while  $A_v$  and  $B_v$  are the incident and reflected voltage waves on the electrodes as shown in Fig. 2(c).

To evaluate the scattering matrix, the total pressure on both faces  $P_1(t)$  and  $P_2(t)$  as well as the voltage across the electrodes V(t) are written in the form of incident and reflected waves, as shown in Fig. 2(c), in the form

$$P_1(z_1t) = A_1e^{i(\omega t - k_m z_1)} + B_1e^{i(\omega t + k_m z_1)}$$
 (38)

$$P_2(z_2, t) = A_2 e^{i(\omega t - k_m z_2)} + B_2 e^{i(\omega t + k_m z_2)}$$
(39)

$$V(t) = (A_v + B_v)e^{i\omega t} (40)$$

and the acoustic velocities  $(v_1(z_1, t))$  and electric current flowing into the transducer are then given by

$$v_1(z_1, t) = \frac{1}{Z_m} (A_1 e^{i(\omega t - k_m z_1)} - B_1 e^{i(\omega t + k_m z_1)})$$
(41)

$$v_2(z_2, t) = \frac{1}{Z_m} (A_2 e^{i(\omega t - k_m z_2)} - B_2 e^{i(\omega t + k_m z_2)})$$
 (42)

$$I(t) = \frac{A_v - B_v}{Z_e} e^{i\omega t} \tag{43}$$

where  $k_m = (\omega/c_m)$  is the wavenumber of the external medium,  $Z_m = \rho_m c_m$  is the acoustic impedance of the external medium,  $\rho_m$  and  $c_m$  are the mass density and speed of sound in the surrounding medium (surrounding fluid), and  $Z_e$  is an arbitrary reference electric impedance. Applying continuity equations to both the mechanical and electrical interfaces

$$u^{(0,1)}(0,t) = v_1(0,t), \quad u^{(0,1)}(h,t) = -v_2(0,t)$$
(44)  
$$I(t) = \frac{dQ}{dt}$$
(45)

and substituting (38)-(40) in (27), (34), and (44) yields

$$A_{p}Z_{e}\overline{e}\omega(A_{2}+B_{2})e^{ihk}+i(A_{v}-B_{v})e^{ihk}\overline{e}$$

$$+iA_{p}Z_{e}k\omega(A_{u}-B_{u}e^{2ihk})(\overline{e}^{2}+\overline{C}^{D}\overline{\epsilon})=0$$

$$(A_{v}-B_{v})\overline{e}+-iA_{p}Z_{e}\omega\overline{\epsilon}(A_{1}+B_{1})$$

$$+A_{p}Z_{e}k\omega(A_{u}-B_{u})(\overline{e}^{2}+\overline{C}^{D}\overline{\epsilon})=0$$

$$\overline{\epsilon}(A_{v}+B_{v})=(A(-1+e^{-ihk})+B(-1+e^{ihk}))\overline{e}$$

$$-\frac{i(A_{v}-B_{v})h}{A_{p}Z_{e}\omega}$$

$$i\omega A_{p}Z_{m}(A_{u}+B_{u})=A_{1}-B_{1}$$

$$i\omega A_{p}Z_{m}e^{-ihk}(A_{u}+B_{u}e^{2ihk})=-A_{2}+B_{2}$$

$$(46)$$

(46) is then arranged into the matrix form

$$\mathbf{M}_1 \begin{bmatrix} B_1 & B_2 & B_v & A_u & B_u \end{bmatrix}^T = \mathbf{M}_2 \begin{bmatrix} A_1 & A_2 & A_v \end{bmatrix}$$
 (47)

where  $M_1$  and  $M_2$  are  $(5 \times 5)$  and  $(5 \times 3)$  system matrices. The scattering matrix is then given by

$$\mathbf{S} = \mathbf{M}_3 \mathbf{M}_1^{-1} \mathbf{M}_2 \tag{48}$$

where

$$\mathbf{M}_3 = \begin{bmatrix} 1 & 0 & 0 & 0 & 0 \\ 0 & 1 & 0 & 0 & 0 \\ 0 & 0 & 1 & 0 & 0 \end{bmatrix}. \tag{49}$$

## B. Rayleigh Model

The thin rod assumption neglects the lateral inertia of the rod that limits its applicability to rods with very large  $\beta$  values (i.e., very slender rods). The Rayleigh rod theory includes the effect of lateral inertia by assuming the displacement fields for an axisymmetric thin rod to have the form [29]

$$u_z = u(z, t), \quad u_r = -vru^{(1,0)}(z, t), \quad u_\theta = 0$$
 (50)

where  $\nu = C_{13}/(C_{11} + C_{12})$  is Poisson's ratio. This model can be used for transducers with lower aspect ratios up to the limit where radial and shear deformations start affecting the response of the transducer.

As for the thin rod case, the electric potential is assumed to have the form  $\phi(z,t)$ . Equation (50) can then be used alongside (32) to express the strain fields inside the rod by substituting them in (10), which in turn can be used to express the stresses and electric displacements through (3)–(9). Substituting everything into the energy equations (12)–(15), neglecting the shear stresses ( $T_4$  and  $T_5$ ), taking the variation of the integral with respect to u(z,t) and  $\phi(z,t)$ , and performing integration by parts yields the electromechanical governing equations

$$A_p \rho u^{(0,2)}(z,t) = A_p \overline{C} u^{(2,0)}(z,t) + A_p \overline{e} \phi^{(2,0)}(z,t) + I_p v^2 \rho u^{(2,2)}(z,t)$$
(51)

$$\overline{e}u^{(2,0)}(z,t) - \epsilon_{33}\phi^{(2,0)}(z,t) = 0$$
 (52)

and the boundary conditions

$$-A_{p}\overline{C}u^{(1,0)}(z,t) - A_{p}\overline{e}\phi^{(1,0)}(z,t) - I_{p}v^{2}\rho u^{(1,2)}(z,t) + P_{1,2}(t) = 0|_{z=0,h}$$
 (53)

$$\delta u(z,t) = 0|_{z=0,h} \tag{54}$$

$$A_{p}(\overline{e}u^{(1,0)}(z,t) - \epsilon_{33}\phi^{(1,0)}(z,t)) - Q(t) = 0|_{z=0,h}$$
  
$$\delta\phi(z,t) = 0|_{z=0,h}$$
 (55)

where  $I_p$  is the polar moment of inertia of the rod. The electrical equation of motion (52) has the same form as the thin rod case (26), and thus, its solution is also given by (34) except for replacing the modified electric permittivity ( $\overline{\epsilon}$ ) with ( $\epsilon_{33}$ ). Substituting back in (51) yields

$$A_p \rho u^{(0,2)}(z,t) = A_p \overline{C}^D u^{(2,0)}(z,t) + I_p v^2 \rho u^{(2,2)}(z,t). \tag{56}$$

The solution of (56) can be written in the form

$$u(z,t) = (A_u e^{-ikz} + B_u e^{ikz})e^{i\omega t}$$
(57)

where k is given by

$$k = \omega \sqrt{\frac{A_p \rho}{A_p \overline{C}^D - I_p v^2 \rho \omega^2}}.$$
 (58)

As with the thin rod case, the electrical and mechanical interface matching conditions can be used to construct the scattering matrix using (48).

### C. Bishop Model

The Bishop rod theory accounts for the coupling between longitudinal and radial displacements inside the rod through the shear elastic modulus  $C_{44}$ . Following the same energy approach yields slightly more involved governing equations

$$A_{p}\rho u^{(0,2)}(z,t) + C_{44}I_{p}\gamma^{2}u^{(4,0)}(z,t)$$

$$= A_{p}\overline{C}u^{(2,0)}(z,t) + A_{p}\overline{e}\phi^{(2,0)}(z,t) + I_{p}\nu^{2}\rho u^{(2,2)}(z,t)$$
(59)
$$\overline{e}u^{(2,0)}(z,t) - \epsilon_{33}\phi^{(2,0)}(z,t) = 0$$
(60)

and boundary conditions

$$-A_{p}\overline{C}u^{(1,0)}(z,t) - A_{p}\overline{e}\phi^{(1,0)}(z,t) + I_{p}v^{2}(C_{44}u^{(3,0)}(z,t) -\rho u^{(1,2)}(z,t)) + P_{1,2}(t) = 0|_{z=0,h}$$
 (61)

$$u^{(2,0)}(z,t) = 0|_{z=0,h}, \quad \delta u(z,t) = 0|_{z=0,h}$$
 (62)

$$\delta u^{(1,0)}(z,t) = 0|_{z=0,h} \tag{63}$$

$$A_{p}(\overline{e}u^{(1,0)}(z,t) - \epsilon_{33}\phi^{(1,0)}(z,t)) - Q(t) = 0|_{z=0,h}$$
  
$$\delta\phi(z,t) = 0|_{z=0,h}. \tag{64}$$

Again, the electrical governing equations are the same as those obtained from the Rayleigh assumption, yielding a simplified mechanical governing equation in the form

$$A_{p}\rho u^{(0,2)}(z,t) + C_{44}I_{p}\nu^{2}u^{(4,0)}(z,t)$$

$$= A_{p}\overline{C}^{D}u^{(2,0)}(z,t) + I_{p}\nu^{2}\rho u^{(2,2)}(z,t) \quad (65)$$

The solution of (65) can be written in the form

$$u(z,t) = \left(A_{u1}e^{-ik_1z} + B_{u1}e^{ik_1z} + A_{u2}e^{-ik_2z} + B_{u2}e^{ik_2z}\right)e^{i\omega t}$$
(66)

where

$$k_{1,2}^{2} = \frac{\rho I_{p} v^{2} \omega^{2} - A_{p} \overline{C}^{D} - A_{p} \overline{e}^{2}}{2C_{44} I_{p} v^{2}} \pm \frac{\sqrt{4A_{p} C_{44} I_{p} v^{2} \rho \omega^{2} + \left(A_{p} \overline{C}^{D} + \frac{A_{p} \overline{e}^{2}}{\overline{\epsilon}} - I_{p} v^{2} \rho \omega^{2}\right)^{2}}}{2C_{44} I_{p} v^{2}}.$$
(67)

As with the Rayleigh case, the electrical and mechanical interface matching conditions can be used to construct the scattering matrix. The main difference is the additional two mechanical boundary equations introduced in (61)–(63).

The interface matching equations could then be arranged in the matrix form

$$\mathbf{M}_{1}[B_{1} \ B_{2} \ B_{v} \ A_{u1} \ B_{u1} \ A_{u2} \ B_{u2}]^{T} = \mathbf{M}_{2}[A_{1} \ A_{2} \ A_{v}]^{T}$$
(68)

where, in this case,  $M_1$  and  $M_2$  are  $(7 \times 7)$  and  $(7 \times 3)$  system matrices. The scattering matrix is then given by

$$\mathbf{S} = \mathbf{M}_3 \mathbf{M}_1^{-1} \mathbf{M}_2 \tag{69}$$

and

$$M_3 = \begin{bmatrix} 1 & 0 & 0 & 0 & 0 & 0 & 0 \\ 0 & 1 & 0 & 0 & 0 & 0 & 0 \\ 0 & 0 & 1 & 0 & 0 & 0 & 0 \end{bmatrix}. \tag{70}$$

#### D. Infinite Plate Model

When the lateral dimensions of the transducer are much larger than its thickness (very low aspect ratio  $\beta$ ), the lateral strains are neglected compared with the strain in the thickness direction, and only the thickness vibrations of the transducer are taken into consideration, that is

$$u_z = u(z, t)$$
.

Following a similar procedure as the thin rod case and substituting  $S_3 = (du_z/dz) = u^{(1,0)}(z,t)$  into (5) and (9) yields

$$T_3 = C_{33}u^{(1,0)}(z,t) + e_{33}\phi^{(1,0)}(z,t)$$
 (71)

$$D_3 = e_{33}u^{(1,0)}(z,t) - \epsilon_{33}\phi^{(1,0)}(z,t). \tag{72}$$

Substituting (71) and (72) in the energy equations (12)–(15) and then into Hamilton's principle (11) then taking the variation of the integral with respect to u(z,t) and  $\phi(z,t)$  and performing integration by parts yield the electromechanical governing equations

$$\rho u^{(0,2)}(z,t) - C u^{(2,0)}(z,t) + e_{33} \phi^{(2,0)}(z,t) = 0$$
 (73)

$$e_{33}u^{(2,0)}(z,t) - \epsilon_{33}\phi^{(2,0)}(z,t) = 0$$
 (74)

and boundary conditions

$$-A_p(C_{33}u^{(1,0)}(z,t) + e_{33}\phi^{(1,0)}(z,t)) + P_{1,2}(t) = 0|_{z=0,h}$$
(75)

$$\delta u(z,t) = 0|_{z=0,h}$$
 (76)

$$A_p(e_{33}u^{(1,0)}(z,t) - \epsilon_{33}\phi^{(1,0)}(z,t)) - Q(t) = 0|_{z=0,h}$$
 (77)

$$\delta\phi(h,t) = 0|_{z=0,h} \tag{78}$$

which are very similar to (25)–(30) in the thin rod case with the only difference being that the system constants  $(C_{33}, e_{33}, \text{ and } \epsilon_{33})$  are used instead of the reduced constants  $(\overline{C}, \overline{e}, \text{ and } \overline{\epsilon})$ . Since the governing equations have the same form as the thin rod case, the same solution approach could be used to reach the simplified mechanical governing equation in the form

$$\rho u^{(0,2)}(z,t) - C^D u^{(2,0)}(z,t) = 0 \tag{79}$$

where  $C^D = C_{33} + (e_{33}/\epsilon_{33})$  is the stiffness of the plate at constant electric displacement (open-circuit conditions). Assuming the harmonic plane-wave solution in the form

$$u(z,t) = A_u e^{i(\omega t - kz)} + B_u e^{i(\omega t + kz)}$$

$$k = \frac{\omega}{c_1}$$
(80)

where  $c_1 = (C^D/\rho)^{1/2}$  is the bulk speed of sound in the plate and  $A_u$  and  $B_u$  are the complex amplitudes of the forward and backward traveling displacement waves.

As with the thin rod case, the electrical and mechanical interface matching conditions can be used to construct the scattering matrix using (48). It should be noted that the scattering matrix obtained in this case would be identical to that expressed by considering both KLM and Mason's thickness expander-plate equivalent circuits since they are derived from the same assumptions. These assumptions constrain the applicability of these models to certain aspect ratios for the transducer, which is investigated in Section III.

# III. RESULTING DYNAMICS AND COMPARISON OF THE ANALYTICAL MODELS

The accuracy of the analytical model predictions is investigated through comparisons to FEM simulations and experimental measurements of the impedance of PZT transducers with different aspect ratios under different loading conditions.

## A. Numerical Model

COMSOL Multiphysics [32] was used to construct a 2-D axisymmetric model for a cylindrical piezoelectric transducer. A coupled multiphysics model was constructed to model the behavior of the transducer both in vacuo (air)<sup>1</sup> and submerged in a fluid (water/oil). Piezoelectric elements that include direct structural-electrostatic coupling were used to discretize the transducer, and acoustic elements were used for the medium surrounding the transducer. Both domains were discretized using a free triangular mesh with ten elements per wavelength of the generated acoustic waves inside the fluid medium. This ensures accurate sampling of the waves in all domains, since the wavelength inside PZT for both shear and longitudinal waves is larger than the acoustic wavelength in air, water, and oil. The boundaries of the piezoelectric and acoustic domains were coupled to model the acoustic-structure interaction. Furthermore, radiation boundary conditions on the external boundaries of the medium were enforced to minimize reflection from the boundaries and simulate an infinite medium. The voltage of the nodes on each face of the transducer was coupled together and connected to lumped electrical circuit elements to model the electrical connections to the transducer (i.e., a voltage supply when the transducer is used as a TX and a load resistance when used as a receiver).

## B. Experimental Validation

The electrical impedance of two cylindrical piezoelectric transducers, manufactured by Steiner and Martins Inc., was measured both in air and in oil using a Solartron SI 1260 impedance analyzer. Since the impedance of air is much smaller than that of piezoelectric ceramics, measurement in air represents free boundary conditions on the transducer. Oil, being an electrically nonconductive fluid, was selected to avoid adding insulating layers to the transducer, which might have affected its performance. The dimensions of the first transducer were 10 mm in diameter and 25 mm in height ( $\beta = 5$ ) to represent a moderately thick rod, while the second one had a 14 mm in diameter and 12 mm in height  $(\beta = 1.7)$  representing a cylinder of moderate diameter to height. Both transducers were made of a modified PZT-5 with a thin layer of silver electrodes on each circular face. Thin wires were soldered to the edge of each electrode to connect the transducers to the signal analyzer. The same wires were used to suspend the transducers both in air and in oil. The impedance was recorded at each frequency and averaged over an integration time of 0.2 s with a linear frequency spacing of 500 Hz. The mass density and dielectric permittivity

<sup>&</sup>lt;sup>1</sup>Note that for these stiff piezoelectric transducers, air (in the experiments) is a good approximation of in vacuo condition.

TABLE I
MEASURED/IDENTIFIED MATERIAL PROPERTIES OF MODIFIED PZT-5

Property	$\rho$	$C_{11}$	$C_{12}$	$C_{33}$	$C_{44}$	$e_{31}$	$e_{33}$	$\epsilon_{11}/\epsilon_o$	$\epsilon_{33}/\epsilon_o$	$Q_m$
Unit	kg/m <sup>3</sup>	GPa	GPa	GPa	GPa	C/m <sup>2</sup>	C/m <sup>2</sup>			
Value	7560	139	92	107	22	-7.2	19	1460	1064	156

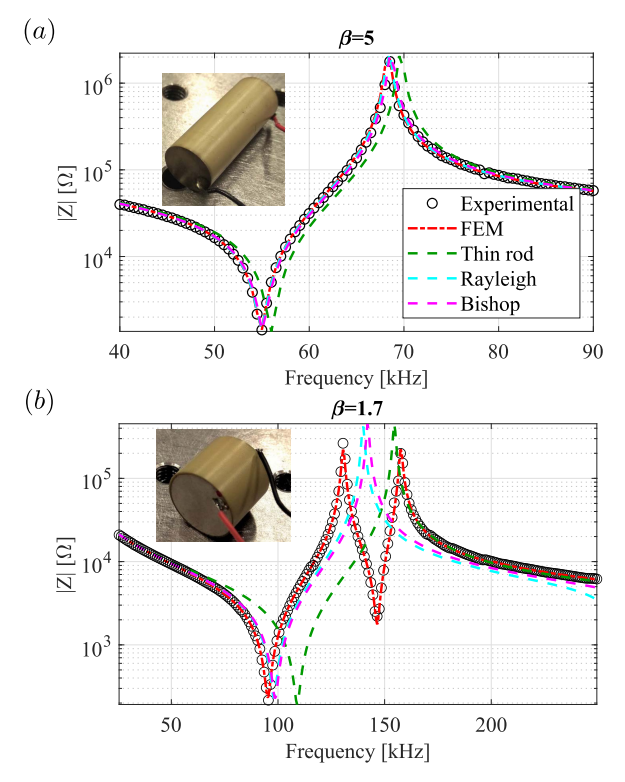


Fig. 3. Comparison of the electrical impedance in air for two cylindrical transducers with aspect ratios. (a)  $\beta=5$ . (b)  $\beta=1.7$ . Experimental results are compared with those estimated numerically using FEM and analytically using thin rod, Rayleigh, and Bishop rod theories.

of the transducers were measured experimentally, and the piezoelectric and elastic constants of the transducers material were identified using a least-squares regression algorithm to fit the FEM to experimental impedance measured for the  $\beta=1.7$  transducer in air. The measured/identified material properties are summarized in Table I.

#### C. Electrical Impedance in Air

Fig. 3 shows the magnitude plot of the electrical impedance in air for both transducers. The results obtained experimentally are compared with that obtained using the numerical and the different analytical models. The boundary conditions for the transducer in air resembles a free–free boundary in the analytical and FEM models. To obtain the impedance of the transducer using FEM, a voltage source was connected between the two electrodes of the transducer, and natural free boundary conditions were applied to all surfaces of the transducer. The results of the analytical model were generated using Qucs open-source circuit simulation package [33]. A voltage source was connected to the electric port (port 3) of the scattering matrix [evaluated from (48) and (69)],

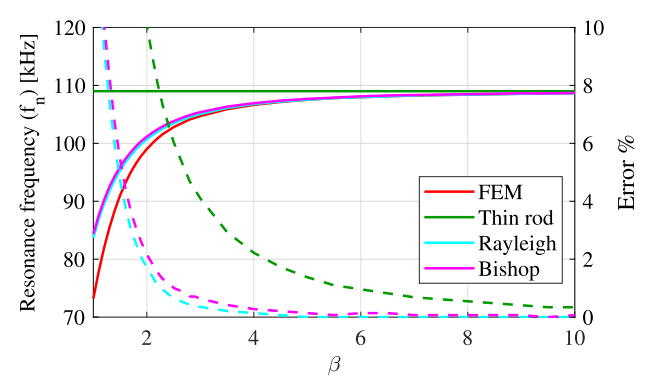


Fig. 4. In-air resonance frequency of the first thickness mode of a PZT transducer ( $h_p=12$  mm) with the variation of the aspect ratio  $\beta$ . Frequency values are shown in solid lines, and percentage errors relative to FEM are shown in dashed lines of the same color.

and the short circuit (zero impedance) was connected to the acoustic ports (ports 1 and 2). To find the impedance for both cases, the applied voltage was divided by the electric current flowing to the transducer.

For the  $\beta=5$  transducer [see Fig. 3(a)], an excellent agreement is observed between the experimental results and FEM, Rayleigh, and Bishop models. The thin rod model for this aspect ratio predicts 2% higher resonance and antiresonance frequencies. This indicates that the effects of lateral inertia cannot be neglected for this aspect ratio or lower. The predictions of both Rayleigh and Bishop models are quite similar, with the relatively simplified Rayleigh model producing slightly more accurate results. This behavior is expected for relatively thin rods since the Rayleigh model tends to better approximate the FEM prediction of a continuous cylinder at low frequencies (around the first mode of the transducer), while it deviates more quickly for higher frequencies [29].

For the  $\beta = 1.7$  transducer [see Fig. 3(b)], only the FEM model perfectly matches the experimental impedance, while all the analytical models predict higher values for the first thickness resonance (95 kHz) of the transducer. While the thin rod approximation is clearly not appropriate anymore for this aspect ratio, predictions of the Rayleigh and Bishop only deviate 3% higher than the FEM value. The analytical models fail to capture the first radial resonance appearing around (146 kHz). This is because all the investigated theories are pure longitudinal theories (with one kinematic variable in the end) and even though the effects of lateral inertia are accounted for in Rayleigh and Bishop models, lateral modes are still not considered in the kinematics of the problem. For this aspect ratio, the lateral and longitudinal modes appear at close frequency ranges, such that more complicated coupled modes start to appear. The accuracy of the analytical predictions when changing  $\beta$  is investigated in Fig. 4. The resonance frequency of the first thickness mode is plotted against  $\beta$  while keeping the transducer height  $h_p = 12$  mm constant. As  $\beta$ approaches one, the effects of lateral inertia start to become more prominent as evident from the shift in the FEM results. Since the Rayleigh and Bishop theories include these effects, they follow the same trend predicted by the FEM up to  $\beta < 2$ ,

where the effects of lateral resonance cause a dramatic increase in the error of both models compared to FEM.

## D. Electrical Impedance in Oil

For most practical applications, thickness-mode transducers are rarely used in air due to the large impedance mismatch between PZT and air. In many applications, either one face of the transducer or the entire transducer is embedded in a solid or liquid domain that would change its dynamic response. To investigate the validity of the analytical models in such conditions, the impedances of the investigated transducers were measured, while the transducers were submerged in soybean oil ( $c=1465\,$  m/s and  $\rho=917\,$  kg/m³) [34]. To capture the effect of fluid loading, the fluid domain around the transducer was included in the simulation, and coupled acoustic-structure boundaries were applied between the structural and acoustic domains.

For the presented analytical models, the presence of the transducer in a fluid domain is accounted for using the unbaffled acoustic radiation impedance  $Z_{\rm rad}$  present on the two acoustic ports. The value of this impedance represents the effect of the fluid on the two circular faces of the transducer. This is compared with the simpler baffled radiation impedance case, where the circular face of the transducer is surrounded by a hard baffle, i.e., the transducer is radiating into only a half-space.

The radiation impedance appearing on a circular radiator depends mainly on the relation between the wavenumber inside the fluid  $(k_m)$  and the radius of the radiator (a). Simple approximate formulas for the unbaffled radiation impedance only exist for the cases where  $k_m a \ll 1$  and  $k_m a \gg 1$ . For the investigated aspect ratios,  $k_m a$  is 1.14 and 2.9 for  $\beta = 5$  and  $\beta = 1.7$ , respectively, which does not allow using such approximations. In this case, the radiation impedance becomes too complicated to be expressed analytically, since the pressure field generated by the transducer is not only dependent on the circular face but is also affected by those generated from the lateral side as well as the back face of the transducer. Neglecting the interactions between the back and lateral sides of the transducer, the radiation impedance can be estimated from [35]. The resulting formula is complicated, and usually, normalized plots [36] are used directly instead of the formula itself.

The effect of fluid loading on the electrical impedance of both transducers is shown in Fig. 5. For both transducers, a very good agreement is observed between the experimental and FEM results. Since lateral fluid loading is neglected, the analytical models predict higher/sharper resonance values when the value of  $\beta$  is small enough for lateral stresses to be substantial but not too small that the lateral surface area becomes negligible. Generally, for  $\beta > 10$  or  $\beta < 0.1$ , the effect of lateral fluid loading is very small and could be safely ignored.

# IV. EFFECT OF ASPECT RATIO ON THE PERFORMANCE OF A THICKNESS-MODE TRANSMITTER

When the transducer is operating as a transmitter, the main design objective is to provide directionally focused ultrasonic

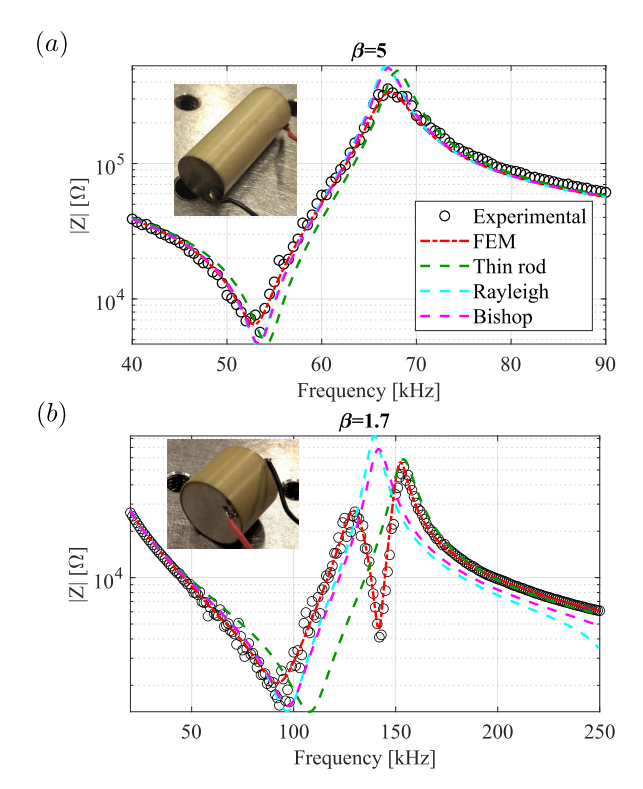


Fig. 5. Comparison of electrical impedance in oil for two cylindrical transducers with aspect ratios. (a)  $\beta = 5$ . (b)  $\beta = 1.7$ . Experimental results are compared with those estimated numerically and analytically.

waves at the maximum allowed level toward the receiver. Usually, within practical limitations, the size of the TX is less constrained than the size of the receiver. Also, the boundary conditions of the transmitter (sideloading/backing) are often easier to control than those of the receiver. For resonant operating transducers, surrounding the back and sides of the transducer with air seems to be the best approach to maximize the energy generated at the front face of the TX [20], [37]. For many energy transfer applications such as biomedical implementations and those involving solid (e.g., metal) walls, this represents the easiest approach as the TX is usually naturally surrounded by air. Consequently, the TX is connected to the medium through one face only, which makes it easy to create a hard baffle around this face to maximize the energy transferred toward the receiver and improve the directionality of the generated acoustic beam. This also facilitates the analytical modeling of the TX since free boundary conditions could be assumed on the back and sides of the transducer. The coupled performance of the transducer is then easily analyzed analytically by connecting a voltage source to the electrical port (port 3), assuming one of the acoustic ports (port 1) to be free (short circuit/zero impedance) and applying the baffled piston radiation impedance to the other acoustic port (port 2). The radiation impedance of a baffled piston  $(Z_{rad})$  is readily available in the literature in the form [38]

$$Z_{\text{rad}} = Z_m \left( 1 - \frac{J_1(2k_m a)}{k_m a} + j \frac{H_1(2k_m a)}{k_m a} \right)$$
 (81)

where  $J_1$  and  $H_1$  are the first-order Bessel and Struve functions. The surface velocity of port 2 represented by the current

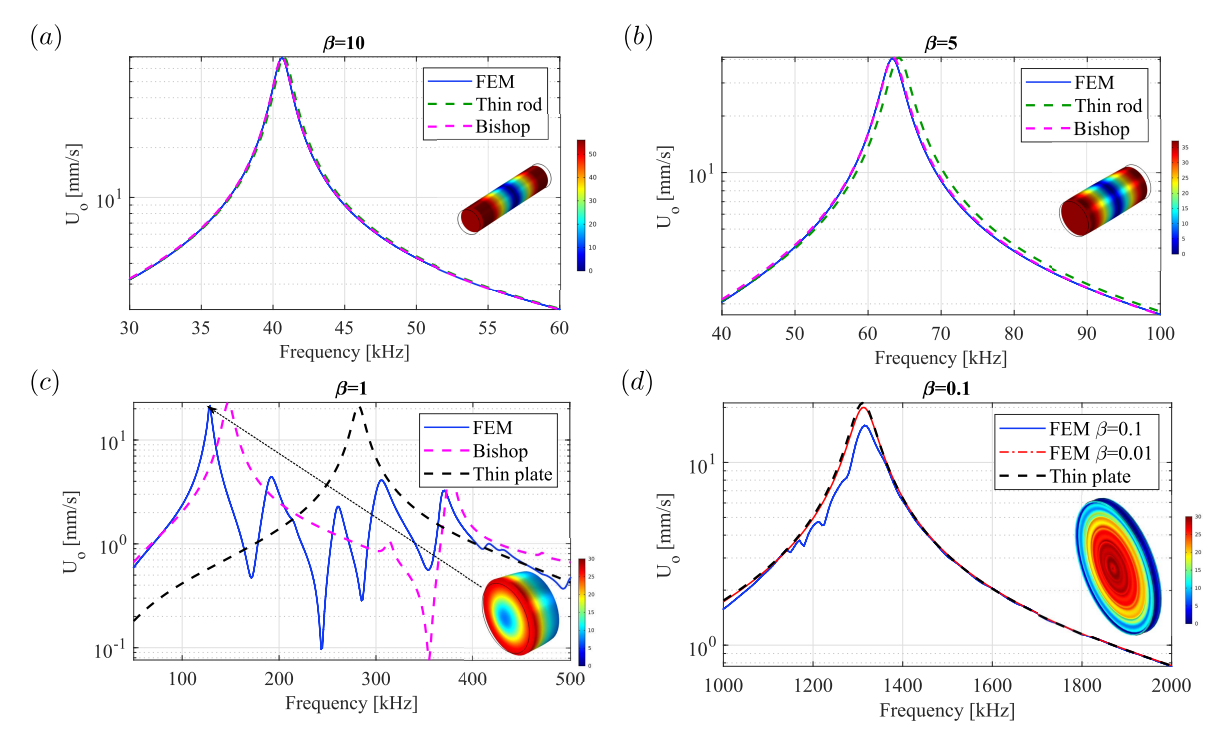


Fig. 6. Effect of aspect ratio on the average normal surface velocity of the transducers. The aspect ratio is varied between (a)  $\beta = 10$ , (b)  $\beta = 5$ , (c)  $\beta = 1$ , and (d)  $\beta = 0.1$ . Insets: surface plots of the distribution of the surface velocity in the axis direction of the transducer (*z*-direction). In all cases, the applied electric field is the same (1 kV/m).

flowing through  $Z_{\text{rad}}$  could then be used to estimate the pressure field outside the transducer by solving the Rayleigh integral [38]

$$P(r,z) = \frac{i\omega\rho_m U_o}{2\pi} \int_{dS} \frac{e^{-ik_m R}}{R} dS.$$
 (82)

The effect of aspect ratio on the performance of the transducer could be evaluated using two approaches: the height of the transducer could be fixed, and hence its resonance frequency, while its radius is varied to change the aspect ratio. This means that the volume of the transducer would change as its aspect ratio changes. Another approach would be to keep the volume of the transducer fixed and vary the aspect ratio changing the relative values of both its radius and its thickness. Since the efficiency of receivers and energy harvesters is usually characterized by the output power per unit volume of the material, the second approach will be followed. A cylindrical transducer with a constant volume of 1 cm<sup>3</sup> made of modified PZT-5 is considered. The aspect ratio is varied from  $\beta = 10$  (thin rod case) to  $\beta = 5$  (thick rod) to  $\beta = 1$  (comparable height to radius cylinder) to  $\beta = 0.1$  (thick plate).

All the analytical models considered in this work assume that the velocity across the face of the transducer is constant. In general, this is not perfectly accurate as the longitudinal velocity of the surface varies with the radius of the transducer. This behavior is difficult to capture analytically but could be captured in the FEM simulation. In order to compare the analytical predictions with the FEM ones, the average surface velocity of the transducer  $U_o$  is compared in both cases.

Fig. 6 shows the effect of aspect ratio of the transducer at constant volume on the average surface velocity of its face when generating ultrasonic waves in water. For all transducers, the electric field applied to the transducer is kept constant at 1 kV/m (as a convenience), which corresponds to an applied voltage  $v \approx 32, 20, 7, 2$  V for aspect ratios  $\beta = 10, 5, 1, 0.1$ , respectively.

Since the fluid loading of the domain is only applied to the circular face of the transducer, the analytical models capture the effect well for thin and moderately thick rods ( $\beta = 10, 5$ ), as shown in Fig. 6(a) and (b). For moderately thick plates ( $\beta =$ 0.1), the infinite plate approximation captures the resonance of the plate; however, it tends to overestimate the average surface velocity of the transducer, as shown in Fig. 6(d). This happens because, for thick plates, the higher order radial modes affect the first thickness mode, yielding a nonuniform normal velocity on the surface of the transducer, as shown in the inset of Fig. 6(d). Keeping the same thickness and decreasing the aspect ratio further to  $\beta = 0.01$  [also Fig. 6(d)] converges toward the thin plate (infinite plate) approximation; however, this aspect ratio might not be practical, especially for air backed transducers. For  $\beta = 1$  [see Fig. 6(c)], both lateral and longitudinal modes are highly coupled, yielding inaccurate estimations of the normal surface velocity for both the thin plate and Bishop approximations. The longitudinal mode is still dominant in this aspect ratio, as shown in the inset of Fig. 6(c); however, the radial and longitudinal mode coupling results in lower overall surface velocity for this aspect ratio for all the modes.

The near-field pressure plots at resonance calculated using the FEM for the considered aspect ratios are summarized in

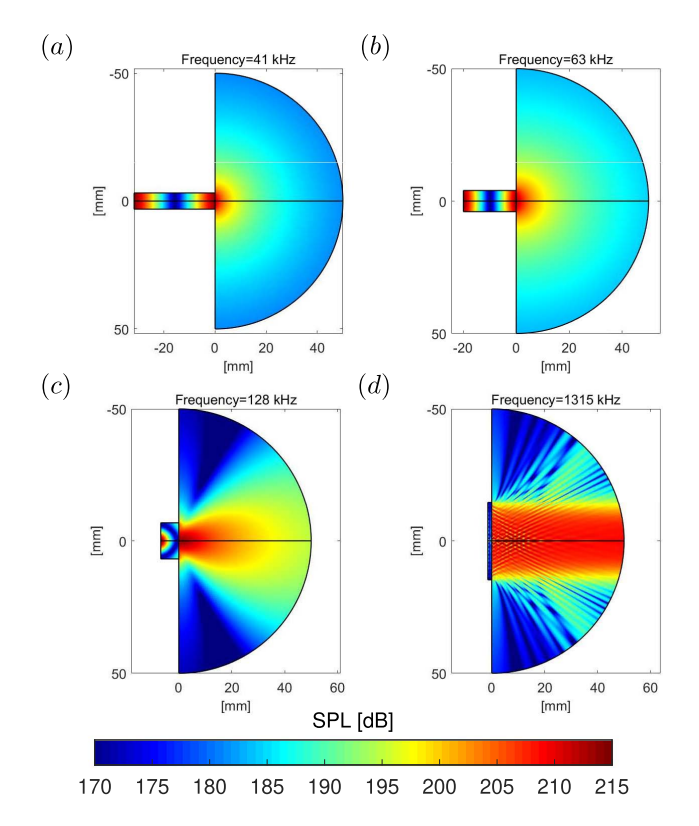


Fig. 7. Effect of aspect ratio on the near-field sound pressure level (SPL) generated by the baffled TX estimated using FEM for (a)  $\beta=10$ , (b)  $\beta=5$ , (c)  $\beta=1$ , and (d)  $\beta=0.1$ . The color contour inside the transducer represents the normalized velocity in the axial direction.

Fig. 7. As the pressure directivity is only controlled by the relationship between the wavelength inside the medium and the radius of the radiator  $k_m a$ , it comes as no surprise that the directivity of the transducer improves with reducing  $\beta$ . For the considered aspect ratios,  $k_m a$  at resonance varies between  $k_m a = 0.6, 1, 3.6$ , and 95.5. This shows that, although the average surface velocity for the thin rod case is relatively higher compared with the other cases, the generated pressure field is almost spherical, and the generated pressure diverges in an open medium making it less suitable for this particular application and perhaps more suitable for applications where the waves could be guided to the RX end.

# V. Effect of Aspect Ratio on the Performance of a Thickness-Mode Receiver

We consider the case in which the RX is completely submerged in an unbounded medium. To focus the analysis on the performance of the transducer, a uniform incident plane wave with an amplitude of  $P_i = 1$  kPa is assumed, and only normal incidence on the circular face of the transducer is considered. Similar to the TX case, a constant volume of 1 cm<sup>3</sup> of modified PZT-5 and the same aspect ratios are considered. The load resistance connected across the electrodes of the transducer is varied across a wide range of resistance values to capture optimum load resistance for maximum power output. The frequency of excitation for each aspect ratio is varied around the expected first longitudinal mode of the transmitter.

The RX case presents a challenge for the analytical models considered here for all aspect ratios. This is because, for rods, fluid loading and pressure incident from the side face cannot be neglected, and for plates, higher order radial modes appear alongside the thickness mode. For the cases where  $\beta \approx 1$ , it is even more involved since the pressure field around the transducer becomes too complicated beyond any analytical approach to the problem. Exceptions to these issues are the extreme cases where the transducer is a very thin long rod  $(\beta \gg 1)$  or a very large thin plate  $(\beta \ll 1)$ ; however, these cases are of limited practical importance for a single thickness-mode receiver.

A numerical approach is the best approach to tackle the RX problem. The FEM model results for the output power for different aspect ratios are shown in Fig. 8. For each aspect ratio, the load resistance was varied to ensure that the peak power output of the RX is captured. It is observed that as  $\beta$  decreases, the optimum load resistance decreases. This is because the capacitance and resonance frequency of the transducer increases with reduced values of  $\beta$ , which decreases the effective electrical impedance of the transducer. It should be noted that for  $\beta = 1$  case, a different trend for the power output is observed when the resistance is higher than the optimum value of 1 k $\Omega$ . Multiple thickness and radial modes are coupled for this aspect ratio, and they are affected by the electromechanical coupling differently. Modes that are better coupled to the electrical domain tend to shift to higher frequencies as the connected resistance increases causing increased bandwidth, but lower amplitude.

The maximum absolute power output among all the considered cases was that of the lowest value for  $\beta$  Fig. 8(d), since the normal area to the incident acoustic intensity is the largest for this case. One might also consider the ratio of the output electric power ( $\Pi_o$ ) to the acoustic power incident normal to the transducer face ( $\Pi_i$ )

$$\Pi_i = \frac{P_i^2 A_p}{2\rho_m c_m}$$

where  $P_i$  is the pressure amplitude of the incident acoustic wave. In this case, the performance of the rod transducer [see Fig. 8(a) and (b)] is found to be better than that of the low  $\beta$  case [see Fig. 8(d)]. The output power for higher values of  $\beta$  is, in fact, higher than the incidence acoustic power on the front face of the transducer. This can be explained by considering Fig. 9, where the power output of the submerged transducer is compared with a flushed transducer where the medium is coupled to the transducer from the front face only. For the  $\beta = 10$  case, the output power is much higher in the submerged case when it is compared with the flushed case. This indicates that the acoustic power is not only captured by the front face but also by the lateral and rear faces of the transducer. In addition, the intensity streamlines (shown in the insets) indicate that the area of the effective acoustic power captured by this aspect ratio is larger than just the normal face area of the transducer. This can be explained by comparing the lateral dimensions of the transducer to the incident wavelength. Since  $k_m a < 1$  for this case, the transducer is effectively a point receiver, and its directivity is almost spherical, as shown

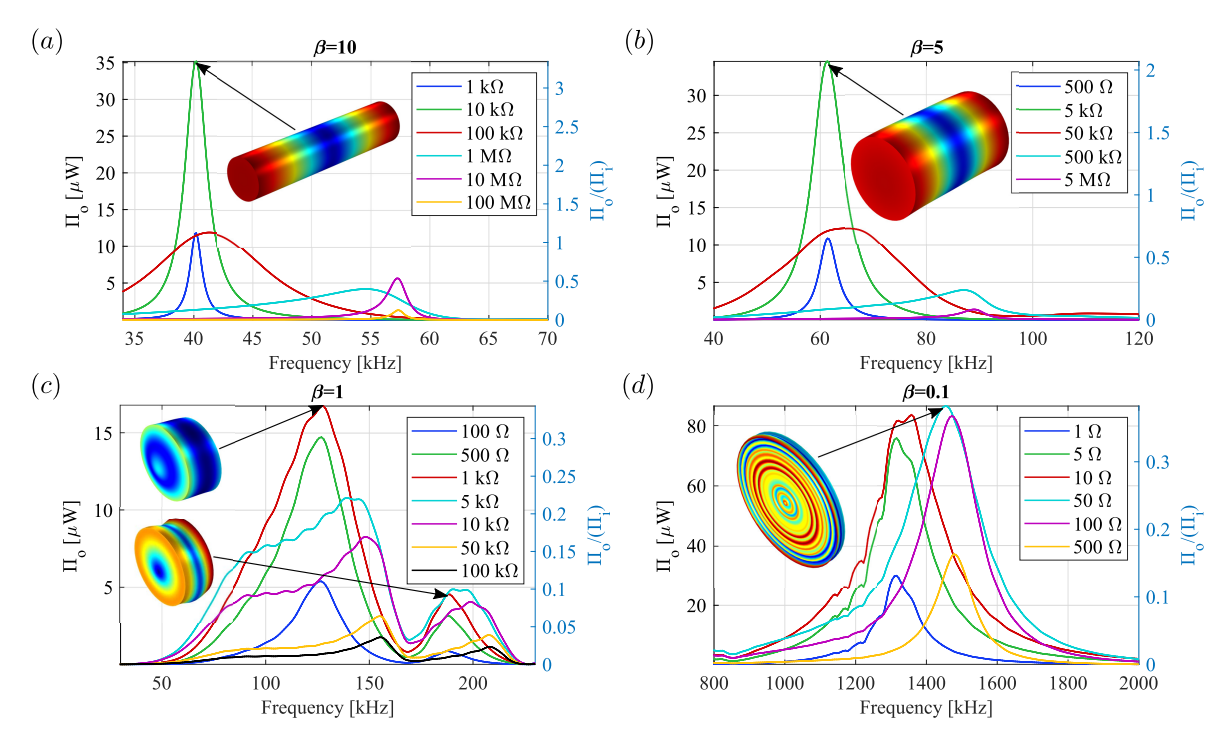


Fig. 8. Effect of the aspect ratio on RX power output of RX for (a)  $\beta = 10$ , (b)  $\beta = 5$ , (c)  $\beta = 1$ , and (d)  $\beta = 0.1$ . The transducers are submerged in water and subjected to incident plane harmonic waves of amplitude (1 kPa) and the power output under different values for the load resistance is estimated using the FEM. Insets: normalized displacement amplitude of the transducers.

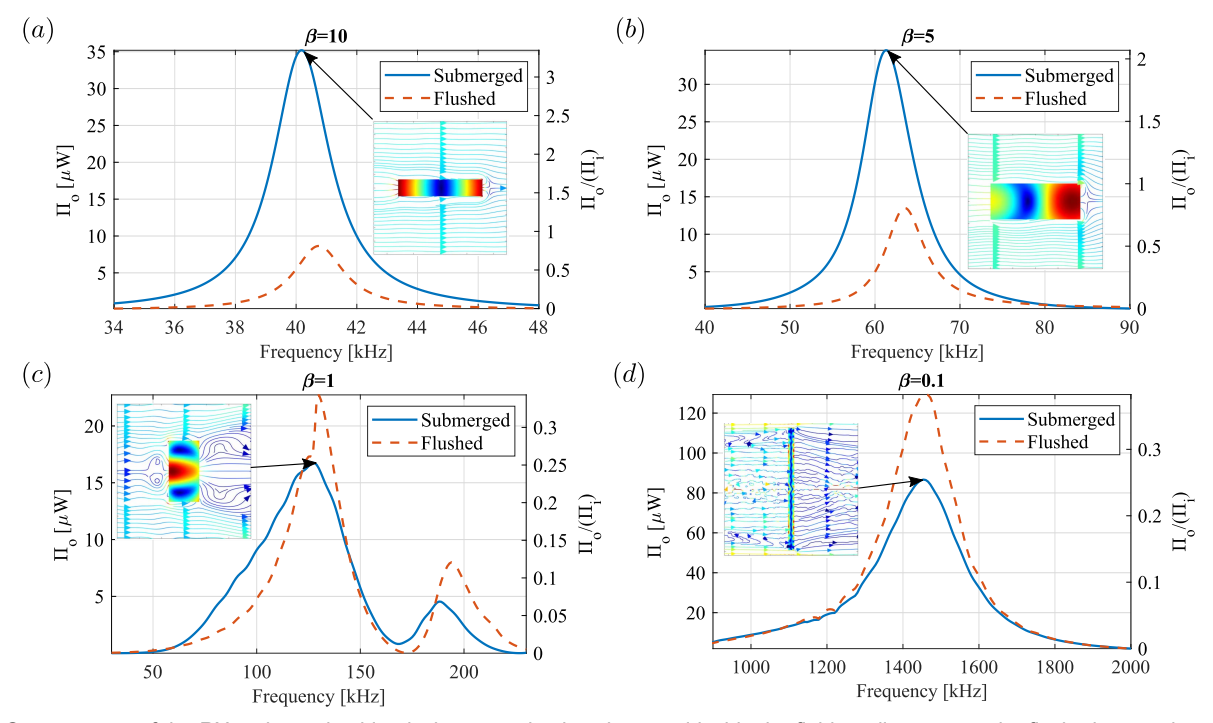


Fig. 9. Output power of the RX at the optimal load when completely submerged inside the fluid medium versus the flushed case where only the front face of the transducer is coupled to the fluid and the other faces are free. The aspect ratio is varied between (a)  $\beta = 10$ , (b)  $\beta = 5$ , (c)  $\beta = 1$ , and (d)  $\beta = 0.1$ . Insets: acoustic intensity streamlines for the submerged case. The normalized displacement amplitude of the transducers is also shown.

in the TX case Fig. 7(a). In comparison, for the  $\beta = 0.1$  case [see Fig. 9(a)], the acoustic power from the submerged case is less than the flushed case. This results from the fact that for the submerged case, the acoustic power is only incident from the front face of the transducer and a portion of it is radiated

from the back face as expected when  $k_m a \gg 1$ . Another aspect to consider is the strength of the longitudinal mode, and how well it is excited by the incident acoustic waves. When considering the maximum absolute power output for the  $\beta = 5$  case, we find that it is smaller than the  $\beta = 10$ 

case even though it has higher normal area intercepting the incident acoustic waves. This is because the longitudinal mode for higher  $\beta$  values is less coupled to the lateral motion and, thus, the incident acoustic waves are converted more efficiently into longitudinal motion and hence generates more electric power. It also explains the degraded peak power output of the  $\beta=1$  case where the longitudinal and lateral motions are strongly coupled, and no dominant mode is observed. As a result, peak power output is smaller compared with all the other cases.

#### VI. CONCLUSION

Several continuum analytical models for estimating the thickness-mode dynamics of a piezoelectric transducer with a cylindrical shape have been investigated with a focus on the effect of aspect ratio. When the radius of the transducer is very small (i.e.,  $\beta > 10$ ), the thin rod analytical model can be used to predict the surface velocity of the transducer around its resonance frequency. The Rayleigh and Bishop rod models can be used to predict the surface velocity of rod transducers with  $(\beta > 3)$  around their resonance frequency, given that the lateral sides of the transducer are not fluid loaded. When the diameter of the transducer is comparable to its length ( $\beta \approx 2$ ), the longitudinal and lateral motion/modes are strongly coupled, and they become difficult to model analytically. Only when the radius of the transducer is very large compared with its thickness ( $\beta$  < 0.1), the thin plate thickness vibration continuum model can be used to describe the behavior of the transducer. All these analytical models cannot predict the effect of fluid loading on the lateral sides of the transducer, which only becomes significant when the diameter of the transducer is comparable to its length. The analytical models are also not accurate for modeling the fluid loaded transducer except for cases with extreme aspect ratios when  $(\beta \gg 1 \text{ or } \beta \ll 1)$ .

For RX applications of the transducers, the electric power generated by a rod-like RX ( $\beta=10$ ) was higher than the acoustic power incident on its front face. The effective receiving area of the transducer was higher than the normal area to the incident acoustic wave. This indicates that arrays of rod-like transducers might be more efficient than a plate-like RX of the same size. Also, since the directivity of the rod-like RX is almost spherical, it would be less sensitive to variations in the angle of incidence of the acoustic beam (e.g., due to the misalignment of the transmitted beam with respect to the RX axis), making it a more effective omnidirectional receiver.

#### REFERENCES

- G. Ottman, H. Hofmann, A. Bhatt, and G. Lesieutre, "Adaptive piezoelectric energy harvesting circuit for wireless remote power supply," *IEEE Trans. Power Electron.*, vol. 17, no. 5, pp. 669–676, Sep. 2002.
- [2] S. Roundy, P. K. Wright, and J. Rabaey, "A study of low level vibrations as a power source for wireless sensor nodes," *Comput. Commun.*, vol. 26, no. 11, pp. 1131–1144, Jul. 2003.
- [3] S. P. Beeby, M. J. Tudor, and N. M. White, "Energy harvesting vibration sources for microsystems applications," *Meas. Sci. Technol.*, vol. 17, no. 12, pp. R175–R195, Dec. 2006.
- [4] P. Mitcheson, E. Yeatman, G. Rao, A. Holmes, and T. Green, "Energy harvesting from human and machine motion for wireless electronic devices," *Proc. IEEE*, vol. 96, no. 9, pp. 1457–1486, Sep. 2008.

- [5] A. Erturk and D. J. Inman, *Piezoelectric Energy Harvesting*. Hoboken, NJ, USA: Wiley, Apr. 2011.
- [6] M. A. Karami and D. J. Inman, "Powering pacemakers from heartbeat vibrations using linear and nonlinear energy harvesters," *Appl. Phys. Lett.*, vol. 100, no. 4, Jan. 2012, Art. no. 042901.
- [7] A. Kurs, A. Karalis, R. Moffatt, J. D. Joannopoulos, P. Fisher, and M. Soljacic, "Wireless power transfer via strongly coupled magnetic resonances," *Science*, vol. 317, no. 5834, pp. 83–86, Jul. 2007.
- [8] S. Li and C. C. Mi, "Wireless power transfer for electric vehicle applications," *IEEE J. Emerg. Sel. Topics Power Electron.*, vol. 3, no. 1, pp. 4–17, Mar. 2015.
- [9] S. Y. R. Hui, W. Zhong, and C. K. Lee, "A critical review of recent progress in mid-range wireless power transfer," *IEEE Trans. Power Electron.*, vol. 29, no. 9, pp. 4500–4511, Sep. 2014.
- [10] M. G. L. Roes, J. L. Duarte, M. A. M. Hendrix, and E. A. Lomonova, "Acoustic energy transfer: A review," *IEEE Trans. Ind. Electron.*, vol. 60, no. 1, pp. 242–248, Jan. 2013.
- [11] A. Christ et al., "Evaluation of wireless resonant power transfer systems with human electromagnetic exposure limits," *IEEE Trans. Electromagn. Compat.*, vol. 55, no. 2, pp. 265–274, Apr. 2013.
- [12] H. Basaeri, D. B. Christensen, and S. Roundy, "A review of acoustic power transfer for bio-medical implants," *Smart Mater. Struct.*, vol. 25, no. 12, Dec. 2016, Art. no. 123001.
- [13] Y. Hu, X. Zhang, J. Yang, and Q. Jiang, "Transmitting electric energy through a metal wall by acoustic waves using piezoelectric transducers," *IEEE Trans. Ultrason., Ferroelectr., Freq. Control*, vol. 50, no. 7, pp. 773–781, Jul. 2003.
- [14] H. F. Leung, B. J. Willis, and A. P. Hu, "Wireless electric power transfer based on acoustic energy through conductive media," in *Proc. 9th IEEE Conf. Ind. Electron. Appl.*, Jun. 2014, pp. 1555–1560.
- [15] C. Lü, J. Yang, J. Wang, and W. Chen, "Power transmission through a hollow cylinder by acoustic waves and piezoelectric transducers with radial polarization," *J. Sound Vib.*, vol. 325, nos. 4–5, pp. 989–999, Sep. 2009.
- [16] M. E. Kiziroglou, D. E. Boyle, S. W. Wright, and E. M. Yeatman, "Acoustic energy transmission in cast iron pipelines," *J. Phys., Conf.*, vol. 660, no. 1, Dec. 2015, Art. no. 012095.
- [17] M. Kiziroglou, D. Boyle, S. Wright, and E. Yeatman, "Acoustic power delivery to pipeline monitoring wireless sensors," *Ultrasonics*, vol. 77, pp. 54–60, May 2017.
- [18] R. Krimholtz, D. Leedom, and G. Matthaei, "New equivalent circuits for elementary piezoelectric transducers," *Electron. Lett.*, vol. 6, no. 13, pp. 398–399, 1970.
- [19] A. Puttmer, P. Hauptmann, R. Lucklum, O. Krause, and B. Henning, "SPICE model for lossy piezoceramic transducers," *IEEE Trans. Ultra-son., Ferroelectr., Freq. Control*, vol. 44, no. 1, pp. 60–66, Jan. 1997.
- [20] S. Ozeri and D. Shmilovitz, "Ultrasonic transcutaneous energy transfer for powering implanted devices," *Ultrasonics*, vol. 50, no. 6, pp. 556–566, May 2010.
- [21] S. H. Song, A. Kim, and B. Ziaie, "Omnidirectional ultrasonic powering for millimeter-scale implantable devices," *IEEE Trans. Biomed. Eng.*, vol. 62, no. 11, pp. 2717–2723, Nov. 2015.
- [22] T.-C. Chou, R. Subramanian, J. Park, and P. P. Mercier, "A miniaturized ultrasonic power delivery system," in *Proc. IEEE Biomed. Circuits Syst. Conf. (BioCAS)*, Oct. 2014, pp. 440–443.
- [23] A. Denisov and E. Yeatman, "Ultrasonic vs. inductive power delivery for miniature biomedical implants," in *Proc. Int. Conf. Body Sensor Netw.*, Jun. 2010, pp. 84–89.
- [24] S. Shahab, M. Gray, and A. Erturk, "Ultrasonic power transfer from a spherical acoustic wave source to a free-free piezoelectric receiver: Modeling and experiment," J. Appl. Phys., vol. 117, no. 10, Mar. 2015, Art. no. 104903.
- [25] S. Shahab, M. Gray, and A. Erturk, "An experimentally validated contactless acoustic energy transfer model with resistive-reactive electrical loading," in *Proc. Act. Passive Smart Struct. Integr. Syst.*, vol. 9431, Apr. 2015, Art. no. 943105.
- [26] M. Gorostiaga, M. C. Wapler, and U. Wallrabe, "Analytic model for ultrasound energy receivers and their optimal electric loads," *Smart Mater. Struct.*, vol. 26, no. 8, Aug. 2017, Art. no. 085003.
- [27] M. Gorostiaga, M. C. Wapler, and U. Wallrabe, "Analytic model for ultrasound energy receivers and their optimal electric loads II: Experimental validation," *Smart Mater. Struct.*, vol. 26, no. 10, Oct. 2017, Art. no. 105021.
- [28] A. Allam, K. Sabra, and A. Erturk, "Comparison of various models for piezoelectric receivers in wireless acoustic power transfer," Act. Passive Smart Struct. Integr. Syst., vol. 10967, Mar. 2019, Art. no. 109670S.

- [29] M. Shatalov, J. Marais, I. Fedotov, and M. J. Tenkam, "Longitudinal vibration of isotropic solid rods: From classical to modern theories," in *Advances in Computer Science and Engineering*. Rijeka, Croatia: InTech, Dec. 2011.
- [30] H. Tiersten, "Hamilton's principle for linear piezoelectric media," *Proc. IEEE*, vol. 55, no. 8, pp. 1523–1524, Aug. 1967.
- [31] C. L. Dym and I. H. Shames, Solid Mechanics: A Variational Approach. New York, NY, USA: Springer, 2013.
- [32] COMSOL Multiphysics Reference Manual, Version 5.4, COMSOL AB, Stockholm, Sweden, 2018.
- [33] (2019). Ques: Quite Universal Circuit Simulator 0.0.20. [Online]. Available: http://ques.sourceforge.net/
- [34] J. N. Coupland and D. J. Mcclements, "Physical properties of liquid edible oils," J. Amer. Oil Chem. Soc., vol. 74, no. 12, pp. 1559–1564, Dec. 1997.
- [35] T. Nimura and Y. Watanabe, "Effect of a finite circular baffle board on acoustic radiation," J. Acoust. Soc. Amer., vol. 25, no. 1, pp. 76–80, Jan. 1953.
- [36] L. L. Beranek and T. J. Mellow, Acoustics: Sound Fields and Transducers, 1st ed. Amsterdam, The Netherlands: Academic Press, 2012.
- [37] G. Kossoff, "The effects of backing and matching on the performance of piezoelectric ceramic transducers," *IEEE Trans. Sonics Ultrason.*, vol. SU-13, no. 1, pp. 20–30, Mar. 1966.
- [38] L. E. Kinsler, Ed., Fundamentals of Acoustics, 4th ed. New York, NY, USA: Wiley, 2000.



Ahmed Allam received the M.Sc. degree in mechanical engineering from Ain Shams University, Cairo, Egypt, in 2017. He is currently pursuing the Ph.D. degree with the G. W. Woodruff School of Mechanical Engineering, Georgia Institute of Technology, Atlanta, GA, USA.

His research interests include acoustic metamaterials, elastic wave propagation, and smart materials.



**Karim G. Sabra** received the Ph.D. degree from the University of Michigan at Ann Arbor, Ann Arbor, MI, USA, in 2003.

He was a Postdoctoral Researcher and then a Project Scientist at the Marine Physical Laboratory, Scripps Institute of Oceanography, University of California at San Diego, La Jolla, CA, USA. He is currently a Professor of mechanical engineering with the Georgia Institute of Technology, Atlanta, GA, USA. He teaches and performs interdisciplinary research on acoustic and elastic

wave propagation with an emphasis on underwater acoustics and signal processing.

Dr. Sabra was a fellow of the Acoustical Society of America (ASA) in 2007. His awards include the 2009 A. B. Wood Medal from the Institute of Acoustics, U.K., the 2011 R. B. Lindsay Award, and the 2015 Medwin Prize in Acoustical Oceanography from the ASA. He is also an Associate Editor of the *Journal of the ASA*.



**Alper Erturk** received the Ph.D. degree in engineering mechanics from Virginia Tech, Blacksburg, VA, USA, in 2009.

He is currently the Woodruff Professor with the G. W. Woodruff School of Mechanical Engineering, Georgia Institute of Technology, Atlanta, GA, USA, where he leads the Smart Structures and Dynamical Systems Laboratory. He has published two books and more than 200 articles in journals and conference proceedings on topics spanning from vibration energy harvesting and

bioinspired actuation to elastic/acoustic metamaterials and phononic crystals.

Dr. Erturk is a fellow of the American Society of Mechanical Engineers (ASME). He was a recipient of various awards, including the NSF CAREER Award in 2013, the ASME Gary Anderson Early Achievement Award in 2015, the ASME C.D. Mote Jr. Early Career Award in 2017, and the SEM J.W. Dally Young Investigator Award (2020), among others.